Structural and magnetic properties of the perovskites $A_2LaFe_2SbO_9$ (A = Ca, Sr, Ba)

Structural and Magnetic Properties of the Perovskites $A_2LaFe_2SbO_9$ (A = Ca, Sr, Ba)

Mylène Hendrickx[1], Yawei Tang[2], Emily C Hunter[2], Peter D. Battle[2] and Joke Hadermann[1]

[1]*EMAT, University of Antwerp, Groenenborgerlaan 171, 2020 Antwerp, Belgium*

[2]*Inorganic Chemistry Laboratory, University of Oxford, South Parks Road, Oxford OX1 3QR, U.K.*

Abstract

Polycrystalline samples of $A_2LaFe_2SbO_9$ (A = Ca, Sr, Ba) perovskites appeared monophasic to X-ray or neutron powder diffraction but a single-crystal study utilising transmission electron microscopy revealed a greater level of complexity. Although local charge balance is maintained, compositional and structural variations are present among and within the submicron-sized crystals. Despite the inhomogeneity, A = Ca is monophasic with a partially-ordered distribution of Fe^{3+} and Sb^{5+} cations across two crystallographically-distinct octahedral sites, *i.e.* $Ca_2La(Fe_{1.25}Sb_{0.25})_{2d}(Fe_{0.75}Sb_{0.75})_{2c}O_9$. For A = Sr or Ba, the inhomogeneities result in differences in the tilting patterns of the octahedra and the ordering of the B cations. Particles of A = Sr contain a phase (Fe:Sb ~2:1) without B cation ordering and one (Fe:Sb ~1:1) with B cation ordering. Monophasic A = Ba lacks long-range cation order although ordered nanodomains are present within the disordered phase. The temperature dependence of the magnetic properties of each sample is discussed.

Keywords: Perovskite oxides; Crystal structure; Transmission Electron Microscopy; Structural variations; Compositional inhomogeneity; Magnetic properties

* Corresponding author: Mylène Hendrickx

Email address: mylene.hendrickx@uantwerpen.be

1. Introduction

Materials with the perovskite crystal structure have been studied for many decades because of the wide variety of physical properties they can display [1–4]. The simplest perovskites have the general formula ABO_3, where A is a relatively large cation, such as an alkaline-earth or rare-earth element, that occupies a twelve-coordinate site, and B is a smaller cation, usually that of a transition metal or p-block element, that occupies an octahedrally-coordinated site. The diverse range of properties derives from the ability of the structure to accommodate a wide range of cation substitutions at either the A site, the B site or both; these often result in the use of formulae of the form $AA'BB'O_6$ or $A_2A'B_2B'O_9$ [5–7]. Perovskites can tolerate the resultant, often significant, chemical strain by undergoing slight structural modifications, such as tilting the octahedral in one of a variety of ways [8–10]. The different cation species on the A and B sites can occupy their respective site in an ordered or disordered manner; ordering is most likely to occur when there is a significant difference in size and charge. Consequently, ordering on the B site is observed more often and is of particular interest for its potential to control the crystal structure and magnetic properties of the material [11–16].

An unequal occupation of the two B sites by magnetic cations can generate interesting magnetic behaviour. Such an ordering of the six-coordinate cations can be induced by the presence of relatively large transition-metal cations and smaller pentavalent or hexavalent p-block cations in unequal numbers. We have, for example, previously synthesised $La_3Ni_2SbO_9$ and shown that it behaves as a relaxor ferromagnet [17,18]. This discovery inspired us to investigate other perovskites with comparable compositions. In the case of $SrLa_2Ni_2TeO_9$, a spin-glass phase and a magnetically-ordered phase were found to coexist at low temperatures [19] whereas $Sr_2LaCr_2SbO_9$ [20] is a ferrimagnet below 150 K. These differences in magnetic behaviour are brought about by differences in both the symmetry of the structure and the degree of cation ordering, and it is clear that the magnetic properties of these perovskites depend on the specific combination of cations that is present. In order to examine the effect of introducing d^5: Fe^{3+} cations, we synthesised $Sr_3Fe_2TeO_9$ and found, contrary to previous reports [21,22], that our sample exhibited an unusual mixture of nano-twinned 1:1 and 2:1 cation-ordered regions, with the former, tetragonal phase behaving as spin-glass and the latter, trigonal phase as an antiferromagnet [23]. In a continuation of this work we have now investigated the iron-containing compositions $A_2LaFe_2SbO_9$ (A=Ca, Sr, Ba). In this paper we report the structural and magnetic properties of these three compounds as determined using a combination of magnetometry, electron microscopy, X-ray diffraction and, where appropriate, neutron diffraction.

2. Experimental

Polycrystalline samples of $A_2LaFe_2SbO_9$ (A=Ca, Sr, Ba) were prepared using the standard ceramic method. ACO_3 (A=Ca, Sr, Ba), La_2O_3, Fe_2O_3, and Sb_2O_5 (purity >99.95%) were weighed out in the appropriate stoichiometric ratio and ground together in an agate mortar for 30 minutes to give a homogeneous mixture. La_2O_3 was heated at 800 °C for 24 hours prior to use to ensure it was completely dry. The mixture was then loaded into an alumina crucible and fired at 800 °C for 24 h. It was then quenched to room temperature, reground and pressed into a pellet which was fired in air at 1150 °C for 48 hours and subsequently annealed at 1150 °C for another 48 hours after further grinding. Finally, the furnace was allowed to cool to 800 °C and then the sample was quenched to room temperature.

The dark brown reaction products were initially characterised by X-ray powder diffraction (XRPD) using Cu $K\alpha_1$ radiation. The data, collected at room temperature on a Panalytical X'Pert diffractometer, were analysed using the Rietveld method [24] as implemented in the GSAS [25] program package. The same software was used to analyse data collected in the neutron diffraction experiments described below.

The molar magnetic susceptibilities of these compounds were measured over the temperature range $2 < T/K < 370$ using a Quantum Design MPMS 5000 SQUID magnetometer. Data were collected on warming in a field of 100 Oe after cooling the samples both in the absence of an applied field (zero-field cooled, ZFC) and in the measuring field (field cooled, FC). The isothermal sample magnetisation of each sample was measured as a function of field over the range $-50 < H/kOe < 50$ at 300 and 5 K after cooling in a field of 50 kOe.

The structure and the composition of the three compounds were further studied by transmission electron microscopy (TEM). The specimens for TEM were prepared by dispersing crushed powder in ethanol and depositing a few drops of this solution on a copper grid covered with a holey carbon film. Selected area electron diffraction (SAED) patterns were recorded with a Thermo Fisher Tecnai G2. Low magnification high-angle annular dark-field STEM (HAADF-STEM) images and energy-dispersive X-ray (EDX) maps were acquired with a Thermo Fisher Osiris microscope equipped with a Super-X detector and operated at 200 kV. Atomic-resolution HAADF-STEM images and EDX maps were acquired with a Thermo Fisher Titan 80-300 "cubed" microscope equipped with a Super-X detector and operated at 300 kV.

Neutron powder diffraction data were collected from $Ca_2LaFe_2SbO_9$ at 300 K and 5 K on the GEM time-of-flight diffractometer at the ISIS spallation source, RAL, U.K. The data collected on detector banks at scattering angles, 2θ, of 34.96, 63.62, 91.30 and 154.40 ° were included in the subsequent analysis. Neutron diffraction patterns were collected from $Ba_2LaFe_2SbO_9$ on

the constant-wavelength powder diffractometer D2b at ILL, Grenoble, France. Data were collected at temperatures of 300 and 5 K using a wavelength of 1.594 Å. The peak shape was modelled using the function devised by van Laar and Yelon [26].

3. Results

3.1. Magnetic Properties

The temperature dependence of the dc molar magnetic susceptibilities of the three compounds is shown in **Figure 1**, along with the field dependence of the magnetisation measured at 300 and 5 K. The susceptibility data collected on the three compositions are qualitatively similar, and all three compounds show a maximum in the ZFC susceptibility at ~50 K. However, the ZFC and FC susceptibilities are not equal at 300 K, and this, together with the non-linearity of the M(H) curves collected at 300 K and the presence of a small remanent magnetisation shows that none of the three compounds is a simple paramagnet at this temperature. We note that the difference between the ZFC and FC data is relatively small in the case of $Ba_2LaFe_2SbO_9$. Differences are apparent in the three $M(H)$ curves recorded at 5 K. Those collected for $Ca_2LaFe_2SbO_9$ and $Sr_2LaFe_2SbO_9$ are symmetric, with the strontium compound displaying a broader hysteresis loop and approaching a lower saturation value than the calcium analogue. In the case of the barium analogue, $M(H)$ is asymmetric, and the saturation value is the lowest of the three. The coercive field and remanent magnetisation per formula unit of each compound at 5 K are listed in **Table 1**; H_c increases and M_r decreases as the radius of the alkaline-earth cation increases.

Table 1. Coercive field, H_c, and remanent magnetisation per formula unit, M_r, of $A_2LaFe_2SbO_9$ (A=Ca, Sr, Ba) at 5 K

Compound	H_c (kOe)	M_r (μ_B)
$Ca_2LaFe_2SbO_9$	0.60	0.18
$Sr_2LaFe_2SbO_9$	2.0	0.074
$Ba_2LaFe_2SbO_9$	3.0	0.058

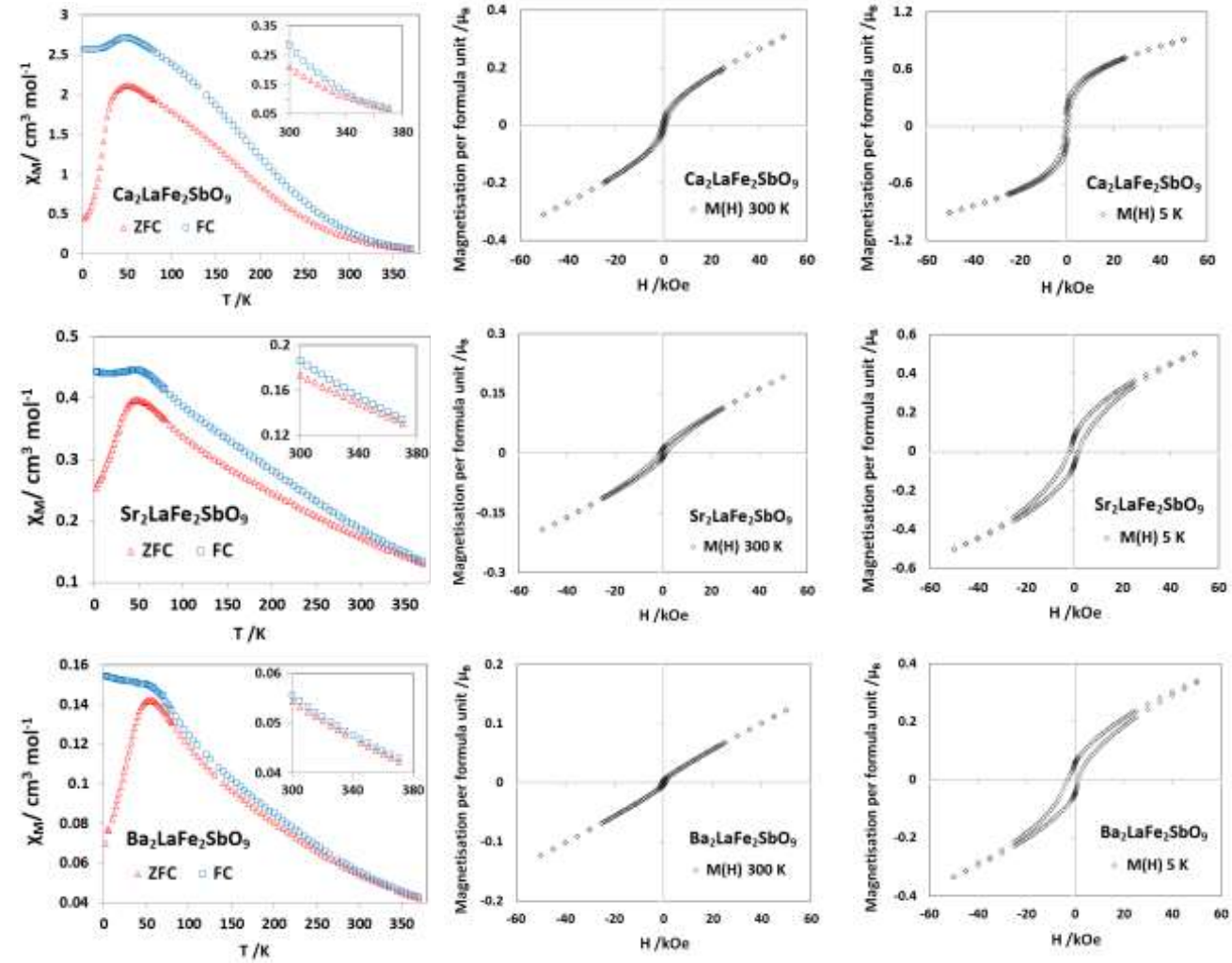

Figure 1. The temperature dependence of the dc molar magnetic susceptibilities and the field dependence of the magnetisation per formula unit of $A_2LaFe_2SbO_9$ at 300 K and 5 K (*A*=Ca, Sr, Ba).

3.2. Structural Chemistry

(i) $Ca_2LaFe_2SbO_9$

The XRPD pattern of $Ca_2LaFe_2SbO_9$ shown in **Figure 2** was indexed using the monoclinic space group $P2_1/n$ with $a \sim\sqrt{2}a_p$, $b \sim\sqrt{2}a_p$ and $c \sim 2a_p$, where a_p is the unit cell parameter of a primitive cubic perovskite. In this space group, the structural model (**Figure 3A)**, involves a 4*f* site that accommodates a disordered distribution of Ca and La, three further 4*f* sites that accommodate oxide anions and two independent B sites, *2d* (½, 0, 0) and *2c* (0, ½, 0) which accommodate the two cation species Fe^{3+} and Sb^{5+}. Refinements of the distribution of Fe and Sb over the crystallographically-distinct B sites suggested that the 2*d* sites are largely occupied by Fe and that the Sb and the remaining Fe atoms are randomly distributed over the 2*c* sites. SAED patterns and the HAADF-STEM images (**Figure 4** and **Figure 5**), confirm the $P2_1/n$ symmetry and cation ordering proposed for $Ca_2LaFe_2SbO_9$ based on the XRPD data. In a HAADF-STEM image, the intensity of the atom columns is proportional to the atomic number of the elements: $I \sim Z^2$. Therefore, the rows with alternation of darker and brighter dots along the *a*-axis correspond to alternating Fe-rich and Sb-rich atom columns, respectively, and show clear ordering of the B cations. The rows with a random distribution of intensities along the *a*-axis correspond to the A site, occupied by calcium and lanthanum in a disordered manner.

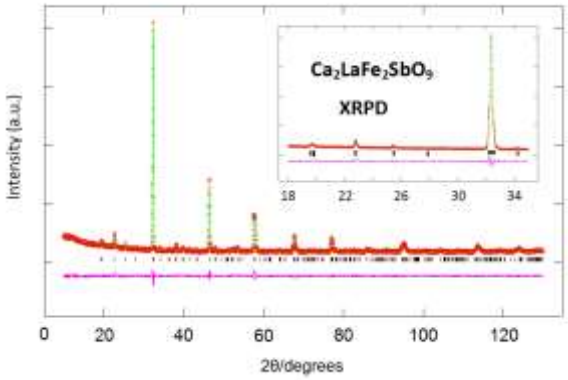

Figure 2. Observed (red), calculated (green) X-ray powder diffraction patterns of $Ca_2LaFe_2SbO_9$ at room temperature. A difference curve (purple) is shown and reflection positions are marked. The low angle region is magnified in the inset.

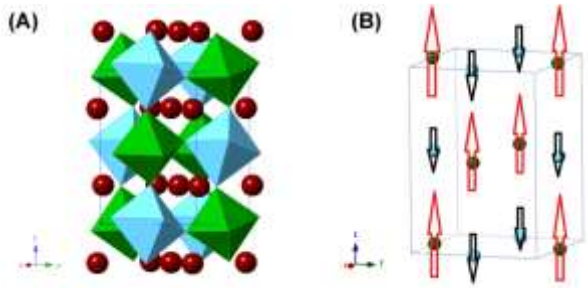

Figure 3. (A) Crystal structure of $Ca_2LaFe_2SbO_9$. Green octahedra are largely occupied by Fe, and blue octahedra are occupied by approximately equal amounts of Fe and Sb. Red circles represent the Ca and La atoms at the A site. **(B)** The G-type magnetic structure adopted by $A_2LaFe_2SbO_9$ (*A*=Ca, Sr, Ba). Arrows indicate the direction of ordered spins at the B sites. Every magnetic ion in the cell is coupled in an antiferromagnetic manner to its six nearest neighbours.

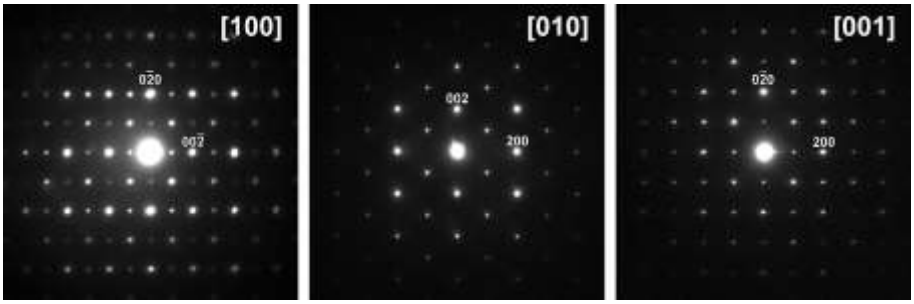

Figure 4. SAED patterns of the $Ca_2LaFe_2SbO_9$ sample along the zone axes [100], [010] and [001] corresponding to the monoclinic $P2_1/n$ symmetry.

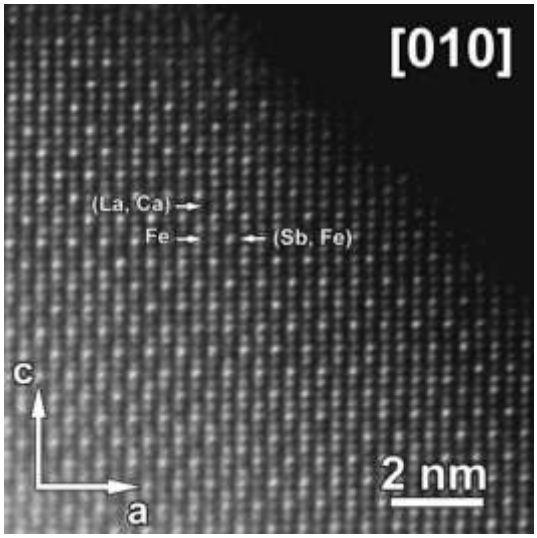

Figure 5. High resolution HAADF-STEM image of $Ca_2LaFe_2SbO_9$ along the [010] zone axis, where the rows with alternation of darker and brighter dots along the *a*-axis correspond to (Fe) and (Sb, Fe) atom columns, respectively. The continuous rows of randomly distributed bright and dark dots along the *a*-axis are occupied by both La and Ca.

Table 2. The average cation content of the $A_2LaFe_2SbO_9$ per element, in percentage of the total cation content, analysed by STEM-EDX based on approximately 45 different regions in at least 25 different particles.

	A	La	Fe	Sb
$Ca_2LaFe_2SbO_9$	34(6)	17(6)	30(3)	19(3)
$Ba_2LaFe_2SbO_9$	34(5)	18(6)	30(3)	18(3)
$Sr_2LaFe_2SbO_9$	30(7)	20(8)	32(5)	18(5)

The average cation content analysed by STEM-EDX based on different particles and regions is given in **Table 2**. The targeted stoichiometry lies within the standard deviation of the average calculated cation composition, but the large standard deviation also indicates an inhomogeneous cation distribution. Supporting information **Figure S1** shows a representative EDX map and confirms this compositional variation across the particles.

The time-of-flight neutron diffraction patterns collected from $Ca_2LaFe_2SbO_9$ at 300 K were analysed using the structural model derived from the XRPD data as a starting point. The magnetic data described above suggest that magnetic Bragg scattering might be present in these patterns and many of the reflections that might be expected to have a magnetic contribution are also sensitive to the degree of cation ordering over the two distinct six-coordinate sites in space group $P2_1/n$. In order to decouple these effects, a combined refinement based on both the neutron pattern and the XRPD pattern was performed. The distribution of Fe and Sb across the 2*d* and 2*c* sites was allowed to vary, and the resulting cation distribution can be represented by the formula $Ca_2La(Fe_{1.25}Sb_{0.25})_{2d}(Fe_{0.75}Sb_{0.75})_{2c}O_9$. The neutron pattern indeed contains additional intensity in the 101 and 011 reflections and in order to account for this intensity it was necessary to include a G-type magnetic structure, see **Figure 3B**, in which the magnetic moment of Fe^{3+} on each B site is coupled in an antiparallel manner to those of the six nearest-neighbour sites. The refined structural parameters and selected bond lengths and angles are listed in **Table 3** and **Table 4**, respectively. The fit to the NPD pattern collected at $2\theta = 34.96$ ° can be seen in **Figure 6A. Figure 6B** shows the fit to the data collected at $2\theta = 154.40$ °, which has a higher resolution but covers a narrower range of *d*-spacing. When we assumed that the Fe^{3+} cations on both sites had the same moment and that all the moments were ordered, then the moment per Fe^{3+} cation was refined to be 1.87(2) μ_B. Given that the Sb^{5+} cation is diamagnetic and the occupancies of Fe on the 2*d* and 2*c* sites are 83.6(4) % and 49.7(4) % respectively, the mean moments per cation on the 2*d* and 2*c* sites were calculated to be 1.56(2) and 0.93(2) μ_B. Analysis of the neutron data thus leads to a description of $Ca_2LaFe_2SbO_9$ as a ferrimagnet at 300 K with a net moment of 0.95(4) μ_B per formula unit.

Analysis of the neutron patterns collected from $Ca_2LaFe_2SbO_9$ at 5 K was carried out using the structural model described above with the cation distribution over the B sites fixed to be the same as that determined from the room temperature data. The observed magnetic scattering is consistent with the G-type structure described above, with the principal change on cooling being an increase in the intensity of the magnetic scattering at higher *d*-spacings. The structural parameters derived from analysis of the data collected at 5 K are listed in **Table 3**, and the bond lengths and bond angles are included in **Table 4**. The fits to the data collected at $2\theta = 34.96$ ° and $2\theta = 154.40$ °, are shown in **Figure 6C**-**D**. With the same assumptions as at 300 K, the mean ordered moment on the 2*d* site at 5 K increased to a value of 2.55(2) μ_B per cation and that on the 2*c* site to 1.52(2) μ_B, leading to a calculated net magnetisation of 1.55(4) μ_B per formula unit at the lower temperature.

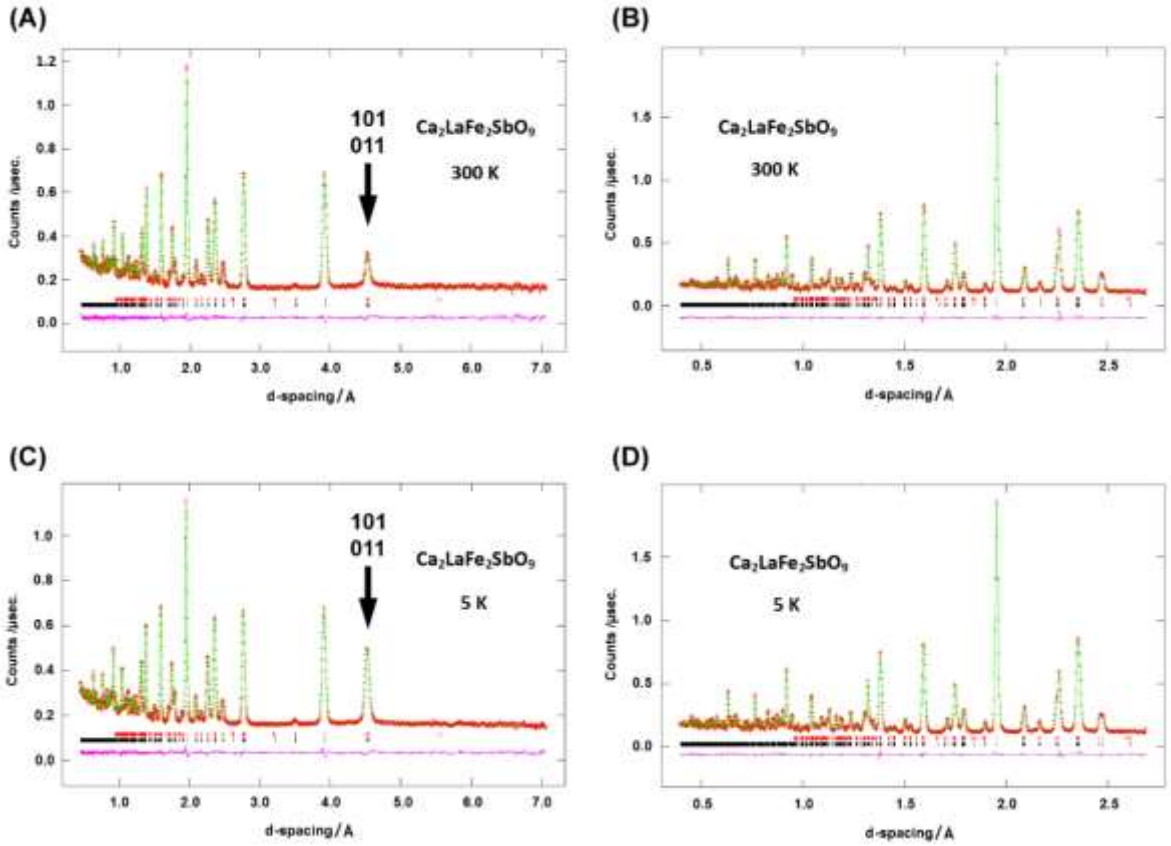

Figure 6. Observed (red), calculated (green) time-of-flight neutron diffraction patterns of $Ca_2LaFe_2SbO_9$ at 300 K collected at **(A)** 2θ = 34.96 ° and **(B)** 2θ = 154.40 ° and at 5 K collected at **(C)** 2θ = 34.96 ° and **(D)** 2θ = 154.40 °. A difference curve (purple) is shown and reflection positions are marked. Black bars represent structural reflections and red bars represent magnetic reflections. The arrows indicate the peak with the strongest magnetic contribution.

Table 3. Structural parameters of $Ca_2LaFe_2SbO_9$ at 300 and 5 K, space group $P2_1/n$

		300 K	5 K
a/Å		5.4967(1)	5.4902(4)
b/Å		5.5466(1)	5.5449(4)
c/Å		7.8079(2)	7.7959(6)
β/º		89.944(5)	89.839(3)
V/Å^3		238.0472(3)	237.3275(8)
R_{wp}/%		3.72	2.26
χ^2		1.6	2.5
Ca/La	x	0.4897(3)	0.4908(3)
4e(x, y, z)	y	0.5330(1)	0.5371(1)
	z	0.2507(4)	0.2512(8)
	U_{iso}/Å^2	0.0122(2)	0.0080(2)
	Ca occupancy	0.6667	0.6667
	La occupancy	0.3333	0.3333
Fe/Sb1	U_{iso}/Å^2	0.0056(6)	0.0036(7)
2*d*(½, 0, 0)	Fe occupancy	0.836(4)	0.836
	Sb occupancy	0.164(4)	0.164
Fe/Sb2	U_{iso}/Å^2	0.0028(6)	0.0025(7)
2*c*(0, ½, 0,)	Fe occupancy	0.497(4)	0.497
	Sb occupancy	0.503(4)	0.503
	M_{Fe} /μ_B	1.87(2)	3.05(2)
O1	x	0.2897(7)	0.2885(6)
4e(x, y, z)	y	0.2894(8)	0.2912(8)
	z	0.0352(3)	0.0387(3)
	U_{iso}/Å^2	0.0066(6)	0.0050(5)
O2	x	0.2092(7)	0.2069(6)
4e(x, y, z)	y	0.7899(8)	0.7887(8)
	z	0.0471(3)	0.0441(4)
	U_{iso}/Å^2	0.0102(8)	0.0072(6)
O3	x	0.5778(2)	0.5805(2)
4e(x, y, z)	y	0.9804(2)	0.9790(2)
	z	0.2496(9)	0.2492(5)
	U_{iso}/Å^2	0.0091(3)	0.0065(2)

Table 4. Selected bond lengths (Å) and bond angles (degrees) in $Ca_2LaFe_2SbO_9$ at 300 and 5 K.

	300 K	5 K
Ca/La – O_1	2.423(3)	2.418(5)
Ca/La – O_1	2.678(4)	2.647(5)
Ca/La – O_1	2.724(4)	2.732(6)
Ca/La – O_2	2.634(4)	2.645(5)
Ca/La – O_2	2.346(3)	2.369(5)
Ca/La – O_2	2.789(4)	2.751(6)
Ca/La – O_3	2.528(1)	2.450(1)
Ca/La – O_3	2.395(2)	2.375(2)
Fe_1/Sb_1 – O_1	1.997(5) * 2	2.011(4) * 2
Fe_1/Sb_1 – O_2	2.012(4) * 2	2.019(4) * 2
Fe_1/Sb_1– O_3	1.998(7) * 2	1.997(4) * 2
Fe_2/Sb_2 – O_1	1.994(4) * 2	1.986(4) * 2
Fe_2/Sb_2 – O_2	2.011(5) * 2	1.993(4) * 2
Fe_2/Sb_2 – O_3	2.004(7) * 2	2.007(4) * 2
O_1 – Fe_1/Sb_1 – O_2	88.9(2)	88.9(2)
O_1 – Fe_1/Sb_1 – O_3	88.05(9)	88.26(8)
O_2 – Fe_1/Sb_1 – O_3	87.8(1)	88.8(1)
O_1 – Fe_2/Sb_2 – O_2	89.2(2)	89.3(2)
O_1 – Fe_2/Sb_2 – O_3	89.8(1)	89.5(1)
O_2 – Fe_2/Sb_2 – O_3	89.2(1)	89.84(9)
Fe_1/Sb_1 – O_1 – Fe_2/Sb_2	156.1(2)	154.9(2)
Fe_1/Sb_1 – O_2 – Fe_2/Sb_2	152.2(2)	153.0(2)
Fe_1/Sb_1 – O_3 – Fe_2/Sb_2	154.51(7)	153.59(7)

(ii) $Sr_2LaFe_2SbO_9$

The XRPD pattern of $Sr_2LaFe_2SbO_9$ (**Figure S2**) could be accounted for in terms of a single perovskite phase having a triclinic unit cell with $a \sim\sqrt{2}a_p$, $b \sim\sqrt{2}a_p$ and $c \sim 2a_p$; the absence of many reflections led us to believe that this cell was *I* centred. However, our subsequent microscopy study revealed that this interpretation of the data was incorrect and that the sample was biphasic.

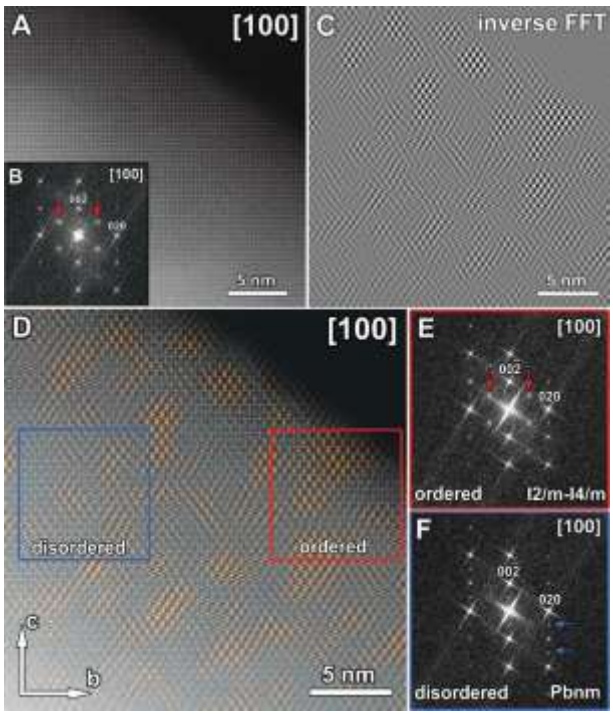

Figure 7.**(A)** High resolution HAADF-STEM image of $Sr_2LaFe_2SbO_9$ along the [100] zone axis. **(B)** The corresponding FFT of the HAADF-STEM image in (A). **(C)** The inverse FFT obtained from the reflections marked by the red arrows in (B). The black and white dots show areas with B cation ordering. **(D)** The original HAADF-STEM image (A) combined with the inverse FFT (C), in which the black and white colors are changed to, respectively, red and yellow using the 'Selective color' function in Adobe Photoshop. The yellow and red dots represent atom columns that contain more Sb and more Fe, respectively. The FFT **(E)** corresponding to the red region can be indexed by the ordered space group *I2/m* or *I4/m*. The FFT **(F)** corresponding to the blue region confirms the disordered *Pbnm* symmetry.

The HAADF-STEM image, shown in **Figure 7**, reveals that the structure has both ordered and disordered regions. **Figures 7A** and **7B** illustrate the original HAADF-STEM image and the corresponding FFT, respectively. **Figure 7C** represents the inverse FFT only taking into account the diffuse intensities marked by the red arrows in **Figure 7B**, which reveals the presence of areas that contain B cation ordering, represented by the ordered black and white dots. The combination of the inverse FFT and the original HAADF-STEM image results in the image shown in **Figure 7D** in which the yellow and red dots correspond to atom columns that contain more Sb or more Fe, respectively. Both phases also occur in large domains or even single phase crystallites. **Figure 8** and **Figure 9** show SAED patterns for domains without and with B cation ordering, respectively; they are consistent with the Fourier transforms shown in **Figures 7F** and **7E.**

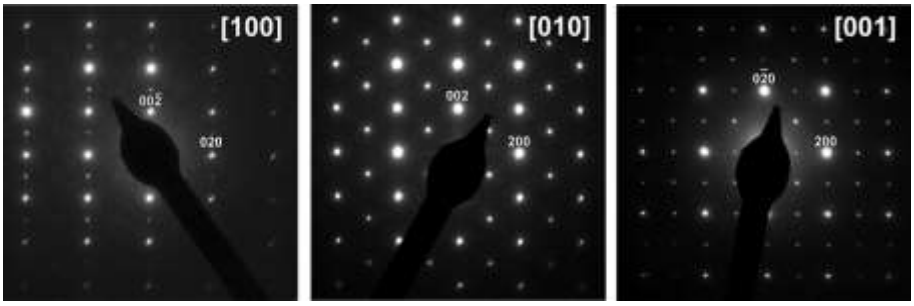

Figure 8. SAED patterns of the $Sr_2LaFe_2SbO_9$ sample along the zone axes [100], [010] and [001] corresponding to the orthorhombic *Pbnm* symmetry.

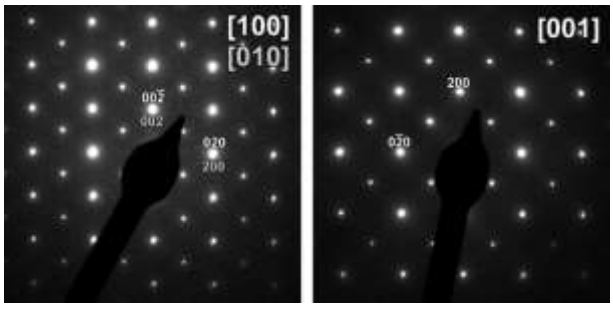

Figure 9. SAED patterns of the $Sr_2LaFe_2SbO_9$ sample along the zone axes [100]/[010] and [001] corresponding to the monoclinic *I2/m* or tetragonal *I4/m* symmetry.

The patterns for the disordered phase could be indexed using the cell parameters: $a \sim\sqrt{2}a_p$, $b \sim\sqrt{2}a_p$ and $c \sim 2a_p$. The reflection conditions derived for the disordered phase are *hkl, hk0: no conditions; 0kl, 0k0: k=2n; h0l, h00: h+l=2n; 00l: l=2n* and indicate the *Pbnm* ($a^-a^-c^+$) symmetry. The combination of these cell parameters with *Pbnm* symmetry indeed indicates a structure with disordered B cations [8,9,27] in this case Fe^{3+} and Sb^{5+}.

The SAED patterns corresponding to the ordered phase (**Figure 9**) can be indexed using several alternative sets of cell parameters and space groups. Possible combinations are cell parameters $a \sim\sqrt{2}a_p$, $b \sim\sqrt{2}a_p$ and $c \sim 2a_p$ with reflection conditions *hkl: h+k+l=2n* corresponding to space groups *I*2/*m* ($a^-a^-c^0$) and *I*4/*m* ($a^0a^0c^-$) [27] (taking into account the B cation order witnessed on the HAADF-STEM), cell parameters $a \sim\sqrt{2}a_p$, $b \sim\sqrt{2}a_p$ and $c \sim 2\sqrt{3}a_p$ with reflection conditions (*hkl* = *hkil* with *i* = *-h-k*) *hkil: -h+k+l=3n; hh0l: h+l=3n: hh2hl: l=3n; 000l: l = 3n* corresponding to space group $R\bar{3}$ ($a^-a^-a^-$) and $a \sim b \sim c \sim 2a_p$ with reflection conditions *hkl: h+k, k+l, h+l=2n* corresponding to space group $Fm\bar{3}m$ ($a^0a^0a^0$). The difference between the structures corresponding to the different space groups is related to the presence of either an anti-phase tilt (denoted with '-') or the absence of a tilt (denoted with '0'). Therefore, we can distinguish between these space groups using images that show the positions of the oxygen atoms that are at the corners of those octahedra. For this, we used ABF-STEM images, as the contrast in such images is proportional to $Z^{1/3}$ of the atom columns and allows visualisation of the light oxygen atoms (Z_O=8) in the presence of heavy elements, whereas HAADF-STEM images do not. **Figure 10** shows an ABF-STEM and HAADF-STEM image of the ordered phase; the red arrows show the upwards and downwards shift of the oxide ions caused by the presence of an octahedral tilt. Consequently, we can exclude the tilt-free ($a^0a^0a^0$) space group *Fm*$\underline{3}$*m*. Furthermore, **Figure 11** shows one of the $<100>_p$ orientations without any tilt, which means that *R*$\underline{3}$*c* ($a^-a^-a^-$) can also be excluded, leaving *I*2/*m* and *I*4/*m* as possible space groups, which would look identical in ABF-STEM images. To distinguish between these two space groups, we should normally use convergent beam electron diffraction (CBED). However the combination of the presence of domains with different phases and twinning and the high degree of similarity between many zones prevents the reliable use of CBED. Therefore, both *I*2/*m* and *I*4/*m* were retained as possible space groups.

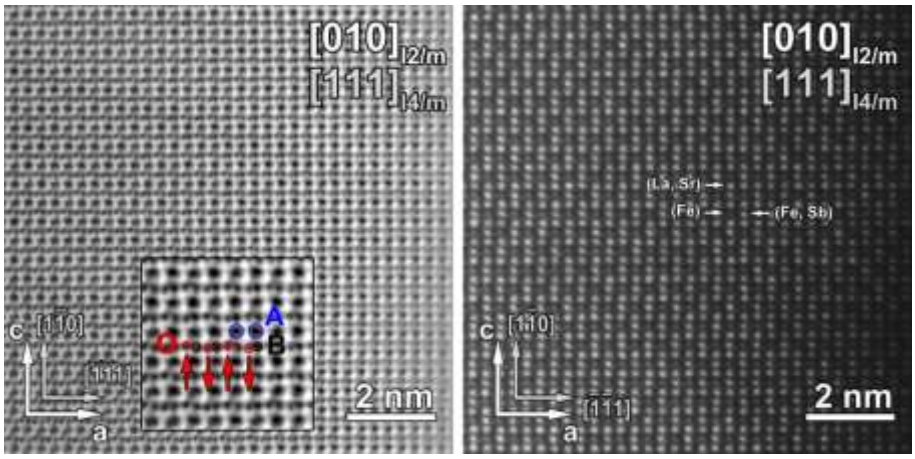

Figure 10. High resolution ABF-STEM (left) and HAADF-STEM (right) image of the ordered phase in $Sr_2LaFe_2SbO_9$ along the [010] or [111] zone axis in respectively *I2/m* or *I4/m*. The red arrows in the ABF-STEM image show the up and downwards shift of the oxygen atom columns along the c direction caused by the presence of an octahedral tilt. The HAADF-STEM image is taken simultaneously with the ABF-STEM image and shows the ordering between the B cations.

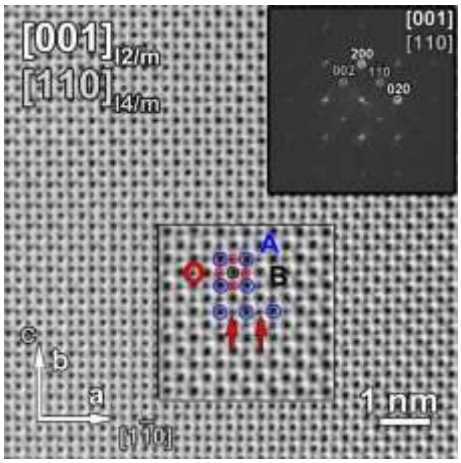

Figure 11. High resolution ABF-STEM image of the ordered phase in $Sr_2LaFe_2SbO_9$ along the [001] zone axis in the *I2/m* symmetry or [110] in the *I4/m* symmetry.

Our subsequent EDX study showed that the coexistence of the ordered and disordered phase is caused by an inhomogeneous distribution of the elements. An elemental map showing the cation distribution in one particle of $Sr_2LaFe_2SbO_9$ is shown in **Figure 12**. In region 1, which corresponds to the ordered phase, the ratio of the A cations (Sr:La) is approximately 4:1 and the ratio of the B cations (Fe:Sb) approximately 1:1, while in the disordered phase (region 2) the Sr:La ratio is closer to 3:2, while the Fe:Sb ration is between 3:2 and 2:1. The average cation content of all analysed particles is given in **Table 2**, which shows that the distribution in this sample is broader than that in the Ca^{2+} and Ba^{2+} analogues. In contrast to the Ca^{2+} (1.34 Å) analogue, the level of inhomogeneity and the difference between the cation size of La^{3+} (1.36 Å) and Sr^{2+} (1.44 Å) are accompanied by phase separation in this material [28]. Our electron diffraction study showed that in some crystallites, the ordered phase is dominant, while in other crystallites, the disordered phase is dominant. Due to the similarity of many zones, we could never exclude the possible presence of the other phase, and we can therefore not conclusively claim that any single phase crystals were present. The coexistence of the two phases, one or both magnetically ordered, with the same basic structure but different symmetries, one of which is uncertain, and with compositions that are ill-defined but different and variable would reduce the accuracy and precision of any parameters derived in a NPD experiment and so none are reported for this compound.

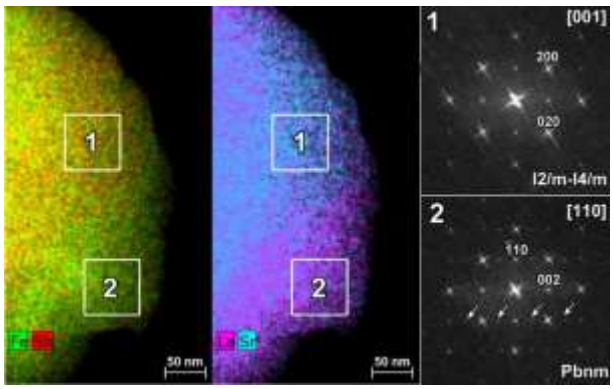

Figure 12. At the left and in the middle the mixed elemental maps of respectively (Fe, Sb) and (La, Sr) are shown, with on the right the FFTs corresponding to region 1 and 2, marked in the elemental maps. The ratio between the cation contents of region 1 is equal to $Sr_{38.5}La_{9.5}Fe_{27.7}Sb_{24.3}O_x$; the cation distribution of region 2 is $Sr_{29.3}La_{20.3}Fe_{32.4}Sb_{18.0}O_x$. The FFT of region 1 is consistent with *I2/m* symmetry, whereas that of region 2 shows extra reflections corresponding to *Pbnm* symmetry.

(iii) $Ba_2LaFe_2SbO_9$

The XRPD pattern of $Ba_2LaFe_2SbO_9$ (**Figure S3**) could be indexed in the space group $Pm\underline{3}m$ with a ~ 4.013 Å, suggesting that this compound adopts the aristotype cubic perovskite structure with Fe^{3+} and Sb^{5+} cations distributed over the six-coordinate sites in a disordered manner. The SAED patterns shown in **Figure 13** are consistent with this model. However, the HAADF-STEM image in **Figure 14** shows the presence of cation-ordered nanodomains. The average cation composition and standard deviation are given in **Table 2**. **Figure S1** shows that for this compound also the exact composition varies within the crystals themselves. However, none of the studied crystallites had the ordered phase as the main phase. As a consequence, we could not determine the exact composition of the main phase and the nanodomains separately. The TEM data for the main phase are not in conflict with space group $Pm\underline{3}m$ but the limited precision and accuracy of cell parameters determined with SAED does not allow us to rule out the following lower-symmetry space groups: $R\underline{3}c$, $I4/mcm$ and $Imma$. These would produce similar diffraction patterns, taking into account possible twinning in the case of the lower symmetries [29]. Similarly, the ordered nanodomains can be described in $Fm\underline{3}m$, $R\underline{3}$, $I4/m$ or $I2/m$.

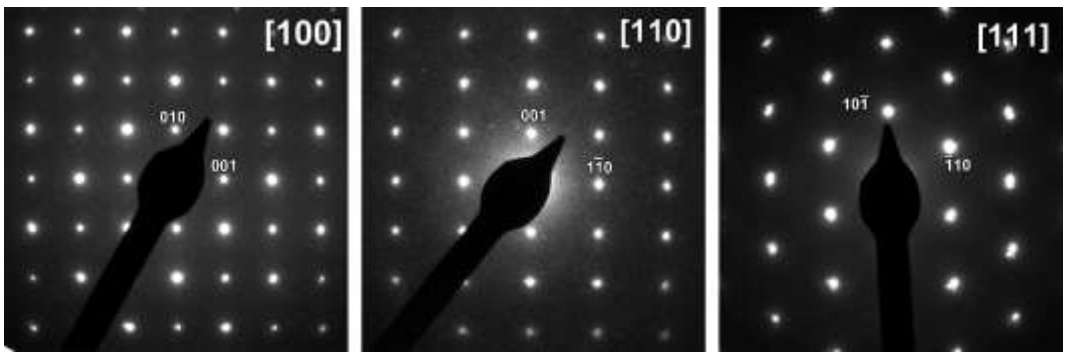

Figure 13. SAED patterns of $Ba_2LaFe_2SbO_9$ sample along the zone axes [100], [110] and [111] corresponding to the cubic $Pm\underline{3}m$ symmetry.

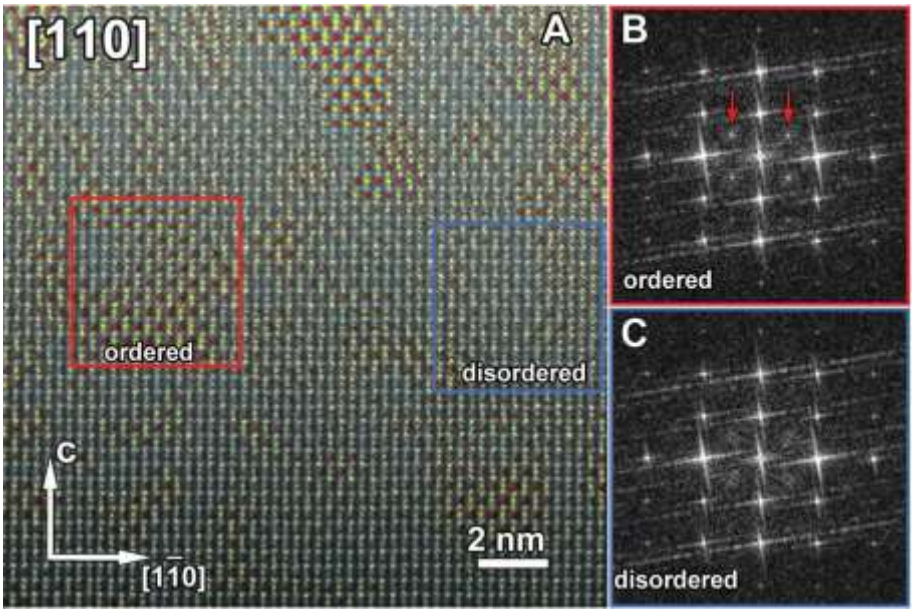

Figure 14. (A) High resolution HAADF-STEM image of $Ba_2LaFe_2SbO_9$ along the [110] zone axis combined with an inverse FFT calculated from the extra reflections marked by the red arrows in (B), in which the black and white colors were replaced by red and yellow in the same manner as for Figure 7. Red therefore indicates a higher Fe content for the column, yellow a higher Sb content, the color alternation visualizes the B cation ordering. **(B)** The extra reflections in the FFT are related to the presence of B cation ordering. **(C)** The B cations are not ordered, and thus no extra reflections appear in the corresponding FFT.

The neutron diffraction pattern collected at 300 K could also be indexed in cubic symmetry although it contained two peaks that could not be indexed under the assumption that the B site cations are disordered. They could, however, be indexed as the 111 and 311 reflections of a $2a_p$ x $2a_p$ x $2a_p$ unit cell. Given that they correspond to relatively large *d*-spacings and were not present in the XRPD or SAED patterns, we assumed that they are magnetic in origin, in which case they signal the presence of G-type antiferromagnetic ordering rather than cation ordering. The reflections indicated by red arrows on the Fourier Transforms of the nanodomains (**Figure 14**) do correspond to the 111 reflections of a $2a_p$ x $2a_p$ x $2a_p$ unit cell but, due to the small size of the nanodomains, it is highly unlikely that the reflections observed by neutron diffraction are caused by the presence of the nanodomains. The structural parameters derived from a Rietveld analysis based on an antiferromagnetic simple cubic model are listed in **Table 5**, and the fitted diffraction pattern is shown in **Figure 15**. As in the case of the calcium-containing sample, the occupancy ratios of the different A- and B-site cations were held fixed at the ideal

value of 2:1. This is justified given the use of stoichiometric mixtures in the synthesis and the absence of any impurity phases in the product. The Bragg peaks are much broader than the instrumental linewidth and have extended Lorentzian tails, consistent with the sample being inhomogeneous over the length scale sampled in a neutron diffraction experiment. No improvement in fit quality was achieved when the symmetry was lowered to rhombohedral, space group $R\underline{3}c$, and we therefore, concluded that the data did not justify the use of a symmetry lower than cubic. Those collected at 5 K were fitted using the same model. The most significant change on cooling was an increase in the magnitude of the ordered magnetic moment, see **Figure 15** and **Table 5**, which was constrained to lie perpendicular to [1 1 1] at both 300 and 5 K.

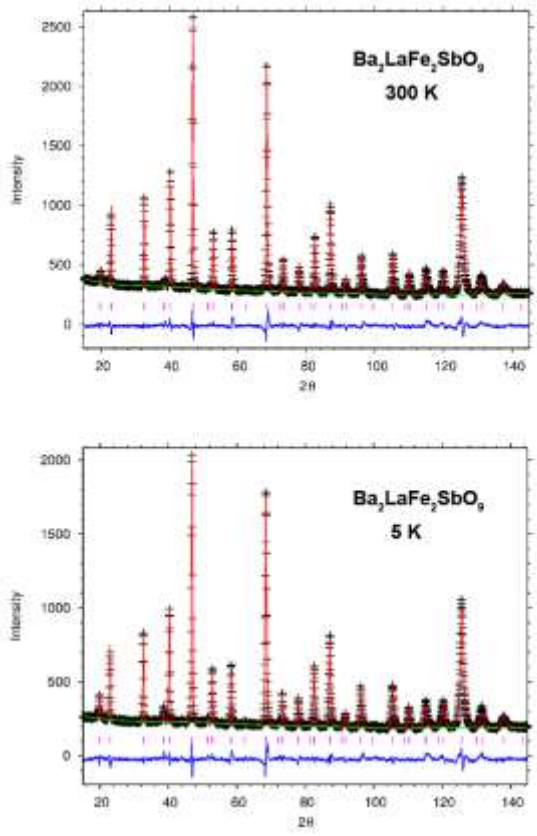

Figure 15. Observed (crosses) and calculated (red line) neutron diffraction patterns of $Ba_2LaFe_2SbO_9$ at 300 and 5 K. A difference curve (blue) is also included. Short vertical lines indicate the positions of reflections that are allowed in either the structural ($Pm\underline{3}m$) unit cell or the magnetic cell with double the volume.

Table 5. Structural parameters of Ba2LaFe2SbO9 at 300 and 5 K. Space group *Pm*$\underline{3}$*m*

		300 K	5 K
a /Å		4.0131(1)	4.0059(1)
V /Å^3		64.63(1)	64.28(1)
$R_{wp\ /\%}$		4.1	4.9
χ^2		5.8	5.4
Ba/La (occupancy 2:1)	U_{iso} /Å^2	0.0057(3)	0.0031(3)
Fe/Sb (occupancy 2:1)	U_{iso} /Å^2	0*	0*
	M_{Fe} /μ_B	1.83(6)	2.70(5)
O	U_{iso} /Å^2	0.0095(2)	0.0078(2)

Ba/La on 1*b* (½, ½, ½); Fe/Sb on 1*a* (0, 0, 0); O on 3*d* (½, 0, 0)

* not refined

4. Discussion

The EDX study revealed that the cation distribution within all three samples is inhomogeneous and an increase of the iron content is accompanied by a local excess of lanthanum in order to maintain local charge neutrality. Scatterplots of the experimental compositions of the three samples are depicted in **Figure 16.** The black dot represents the average composition, showing a deviation from the nominal one, which is marked by a red dot. The sequence of the degree of compositional homogeneity based on the standard deviations calculated from the experimental compositions is $Ba_2LaFe_2SbO_9 \geq Ca_2LaFe_2SbO_9 > Sr_2LaFe_2SbO_9$. However, the difference in standard deviation between $Ba_2LaFe_2SbO_9$ and $Ca_2LaFe_2SbO_9$ is insignificant. The greatest level of compositional inhomogeneity is associated with the sample containing multiple phases. For all three samples, the variation in A and B cations occurs in such a way that each individual domain keeps the same total charge per unit cell as for the average composition. Such conservation of the charge per domain was also seen in the *A*La$_2$Fe*B*SbO$_9$ (*A* = Ca, Sr, Ba; *B* = Ni, Co) series [15]. If we assume that the total content of A cations (La, *A*) per unit cell versus the total content of B cations (Fe, Sb) per unit cell equals 1, since the crystal structure is perovskite, and that the oxygen sites are fully occupied, preservation of the total charge allows to rewrite the composition as $A^{2+}_{<A>-x}La^{3+}_{<La>+x}Fe^{3+}_{<Fe>+x/2}Sb^{5+}_{<Sb>-x/2}O_9^{2-}$ (<element> is the average content of the element). This allows to calculate for each Fe:Sb ratio, which *A*: La ratio would maintain the total charge; this relation is shown as the grey curve in **Figure 16.** The experimental values in the scatterplot indeed closely follow this curve.

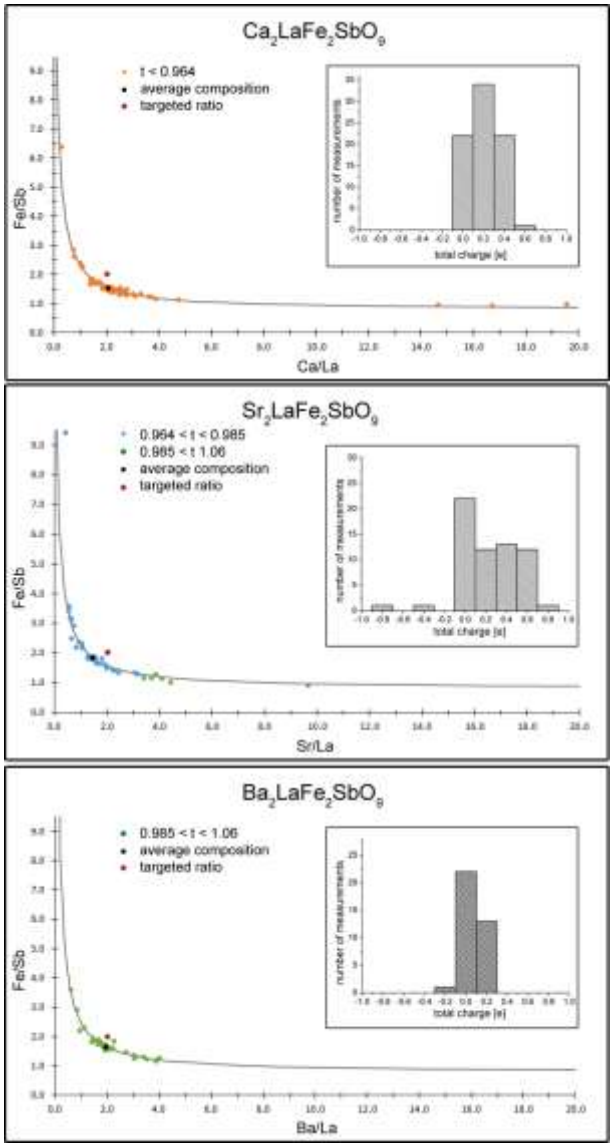

Figure 16. Scatterplots, taken from the experimental compositions obtained from the $A_2LaFe_2SbO_9$ perovskites. The x-axis shows the ratio between the A cations, *A*/La, and the y-axis shows the ratio between the B cations Fe/Sb. The 't' in the legend stands for the calculated tolerance factors. Inset shows the total charge of all the experimental compositions. The grey line represents the relation between the variations of the (*A*, La) and (Fe, Sb) concentrations while preserving the total net charge.

Starting from the average cation content instead of the theoretical targeted one eliminates the influence of possible systematic errors due to different sensitivity to different elements or peak overlap, as here we only aim to study whether the compositional variation follows a clear curve, not what the exact absolute charge is.

The total charge for $Ba_2LaFe_2SbO_9$ lies close to zero, as one would expect, corresponding to a charge balance. For $Ca_2LaFe_2SbO_9$ the total charge is +0.2(1)e, which can be attributed to the

overlap of the K-line of Ca (3.692 keV) and the L-line of Sb (3.604 keV). This does not allow an accurate fitting of the Ca and Sb quantities and possibly resulted in part of the Sb being classified as Ca. This leads to a higher positive net charge for the cations due to the higher oxidation state of Sb^{5+} compared to Ca^{2+}.

In the case of $Sr_2LaFe_2SbO_9$, the total charge is shifted to a positive net charge with an average of ~ 0.3(3)e. Only for this compound, does the measured *A*/La ratio not agree with the targeted *A*/La ratio, i.e. Sr:La ≈ 3:2 instead of 2:1. However, the energy of the X-rays corresponding to the L-line of strontium (1.806 keV) is much lower than the energy of the X-rays corresponding to the lines of La (L-line 4.647 keV), Ca (K-line 3.692 keV), and Ba (L-line 4.466 keV). As low energy X-rays are more likely to be absorbed by the sample [30], the detected X-rays of strontium will suffer more from absorption than the X-rays from the other elements. As a consequence, it might be that the measured strontium content is lower than that present in the sample, causing the positive shift of the net charge and the apparent deviation of the Sr:La ratio from the targeted ratio.

From a structural point of view, $Ca_2LaFe_2SbO_9$ is the simplest of the three compositions described above. The X-ray, neutron and TEM data are all consistent with a monoclinic $P2_1/n$ structure in which the B sites are occupied by a partially-ordered arrangement of Fe^{3+} and Sb^{5+} cations. At room temperature there is very little difference between the mean bond lengths around the two sites but the antimony-rich site is smaller at 5 K. The two sites are also of a similar size in Ca_2FeSbO_6, where the Fe:Sb cation occupancy ratio at the larger B site has been reported to be 94:6 [31].

The structural simplicity of $Ca_2LaFe_2SbO_9$ is emphasised when it is contrasted with $Sr_2LaFe_2SbO_9$. The latter sample was revealed by TEM to contain a broader range of compositions than either of the others, and the scale of the variation was sufficient to cause the sample to separate into two phases with unit cell parameters similar enough for the true nature of the sample not to have been recognised by XRPD; the data produced by that technique could be accounted for using a single phase of lower symmetry. From TEM it was found that $Sr_2LaFe_2SbO_9$ contains two phases: an ordered I-centred phase with space group *I2/m* or *I4/m* with a cation ratio Sr:La ~ 4:1 and Fe:Sb ~ 1:1, and a disordered orthorhombic phase with space group *Pbnm* showing a cation ratio Sr:La ~ 3:2 and Fe:Sb ~ 3:2. This difference in phase separation between $Ca_2LaFe_2SbO_9$ and $Sr_2LaFe_2SbO_9$ could have its origin in the size differences of the A cations: Ca^{2+} and La^{3+} are much closer in size than Sr^{2+} and La^{3+}, so the $Ca_2LaFe_2SbO_9$ structure is more tolerant to variations in composition. For $Sr_2LaFe_2SbO_9$, the La-rich regions likely adopt a structure with more octahedral tilt than Sr-rich regions because

of the smaller A site cation. The crystal structure of the ordered $Sr_2LaFe_2SbO_9$ phase is similar to the structure of Sr_2FeSbO_6 reported by Faik *et al.* [31]

Based on the similarity of the ionic radii of Fe^{3+} and Sb^{5+} and the relatively small difference in charge, the occurrence of ordering, or partial ordering, between Fe^{3+} and Sb^{5+} is more surprising than the occurrence of disorder. We note that no B site cation ordering was detected by neutron diffraction in $SrLaFeSn^{4+}O_6$ [32], $Sr_2FeTa^{5+}O_6$ [33] or $Sr_2FeNb^{5+}O_6$ [34] although two different ordered phases were seen in $Sr_3Fe_2Te^{6+}O_9$ [23].

Finally, for $Ba_2LaFe_2SbO_9$ the TEM study confirmed the disordered cubic $Pm\underline{3}m$ structure, but also revealed a low concentration of ordered nanodomains with $Fm\underline{3}m$ symmetry. The broad peaks and tails observed in the NPD pattern are consistent with the occurrence of these ordered nanodomains.

We also calculated the tolerance factors from the observed compositions for each crystallite to predict the symmetries. The detailed discussion can be found in the supporting information. For the Ca and Ba compounds the predicted symmetries correspond to the experimentally observed ones but for the Sr compound they do not. We believe this is testimony to the fact that the tolerance factor is a useful rough guide but not a strict principle with which to predict accurately the structure.

It appears that the larger the radius ratio r_A/r_B, the more likely the cations are to be disordered [14], with calcium-based compositions tending to order, their strontium analogues adopting both ordered and disordered forms and the barium analogues being disordered. Vasala *et al* [6] have commented on this trend in the past and ascribed it to the greater need to maximise the separation between highly-charged cations when the unit cell volume is reduced.

Our neutron diffraction data show that $Ca_2LaFe_2SbO_9$ and $Ba_2LaFe_2SbO_9$ have a G-type magnetic structure at both room temperature and 5 K. Each Fe^{3+} cation on a 2*c*/2*d* site couples antiferromagnetically to a maximum of six nearest-neighbours (NN) on a 2*d*/2*c* site via a pseudo-linear Fe – O – Fe superexchange pathway. In the case of $Ca_2LaFe_2SbO_9$, the presence of different concentrations of Fe^{3+} cations on the two crystallographic sites apparently results in ferrimagnetism whereas cation disorder in the main phase of $Ba_2LaFe_2SbO_9$ results in equal populations of Fe^{3+} on the two sites and, consequently, antiferromagnetism. However, in both cases, the ordered magnetic moment per cation, see **Table 3** and **Table 5**, is lower than would be expected for a simple Fe^{3+} system. Furthermore, the behaviour of $\chi(T)$, see **Figure 1**, suggests that these are not simple systems. In the case of $Ca_2LaFe_2SbO_9$, hysteresis is apparent

in the susceptibility over the whole of the measured temperature range and a transition is apparent in both the ZFC and FC data at ~40 K. The temperature-independent nature of χ_{FC} and the positive temperature gradient of χ_{ZFC} below this temperature are together reminiscent of a spin glass. In order to account for these data, we propose that at a temperature above the upper limit of our magnetometer, NN Fe^{3+} moments begin to couple in a G-type manner to form ordered ferrimagnetic regions which at 300 K are large enough to give rise to magnetic Bragg scattering. However, at this temperature, not all the atomic moments are coupled to one of these regions as a consequence of the magnetic dilution brought about by the presence of diamagnetic Sb^{5+} cations on both the 2*c* and 2*d* sites. As the temperature decreases, more spins couple to the long-range ordered structure and the mean ordered moment per Fe^{3+} cation increases. However, the low moment measured by neutron diffraction at 5 K and the transition seen in $\chi(T)$ suggest that some spins never order, but instead they freeze at ~40 K to form a glassy phase. By analogy with $Sr_2LaCr_2SbO_9$ [35], we suggest that some of the decoupled spins might lie in the domain walls that separate different ferrimagnetic regions. The domain structure of the material might also be responsible for the failure of $M(H)$, see **Figure 1**, to reach the value of 1.55 μ_B per formula unit predicted by the neutron data. The concentration of magnetic Fe^{3+} cations on the octahedral sites of $Ca_2LaFe_2SbO_9$ is greater than the percolation threshold and it is not immediately obvious why long-range ferrimagnetic ordering does not occur throughout the structure at 5 K. However, we note that Sr_2FeSbO_6 adopts a Type 1 antiferromagnetic structure [15] in which the dominant magnetic interaction is that between next-nearest-neighbour (NNN) cations ~5.5 Å apart. TEM has shown that the local cation composition varies throughout our sample of $Ca_2LaFe_2SbO_9$ and, by analogy with Sr_2FeSbO_6, in antimony-rich regions, there will be competition between the NN and NNN interactions which will lead to frustration and hence the absence of long-range magnetic order. We suggest that it is the spins in these regions that do not belong to the G-type structure favoured by NN interactions and instead undergo a transition to a glassy state at ~40 K. This explanation of $\chi(T)$ for $Ca_2LaFe_2SbO_9$ can be extended to include $Sr_2LaFe_2SbO_9$ where the composition variation is large enough to cause phase separation. We can then qualitatively describe $\chi(T)$ for the strontium analogue as the sum of contributions from iron-rich and antimony-rich regions of the sample, but a more detailed analysis is not possible at this time.

As a result of the random distribution of cations over the six-coordinate sites of $Ba_2LaFe_2SbO_9$, the underlying magnetic structure is that of an antiferromagnet rather than a ferrimagnet. The near-absence of hysteresis in $\chi(T)$ at high temperatures is consistent with this assignment. Once again the low magnitude of the ordered magnetic moment and the formation of a spin glass

below ~50 K indicate that not all of the spins are coupled to the ordered array that extends through the structure and that the antiferromagnetic phase coexists with a spin glass at low temperatures. The level of variation in the composition of $Ba_2LaFe_2SbO_9$ is similar, see **Figure 16** and **Table 2**, to that seen in $Ca_2LaFe_2SbO_9$ and we propose that the observed behaviour is again attributable to frustration caused by competition between NN and NNN neighbours in antimony-rich regions. The ordered nanodomains observed by TEM might be responsible for the hysteresis seen at high temperatures, but this is a somewhat speculative suggestion.

This study was originally motivated by the observation of relaxor ferromagnetism in $La_3Ni_2SbO_9$ [17,18] and subsequently in $La_3Ni_2TaO_9$ [16,36]. We have synthesised a number of triple perovskites containing Cr^{3+} [20] and Fe^{3+} [23,37] in an attempt to find more examples of relaxor behaviour but without success. In many cases, including those described above, we have invoked competition between NN and NNN interactions to explain the observed behaviour of our samples. This leads us to suggest that the relaxor phenomenon is most likely to be observed in compounds containing Ni^{2+} because the d^8:t_{2g}^6 e_g^2 electron configuration leads to a NNN interaction than is weaker than those involving d^3:t_{2g}^3 or d^5:t_{2g}^3 e_g^2 configurations.

5. Conclusion

The three compounds described above exemplify the structural complexities that can exist within the perovskite family. It is possible to synthesise samples whose chemical formulae suggest that multiple elements are present on the six-coordinate site within the structure and it is possible that the XRPD pattern of the sample will be consistent with the formation of a monophasic product. However, TEM can reveal variations in composition, cation ordering and symmetry that are not seen by XRPD and these variations can have a marked effect on the physical properties of the material. It is clearly important to study the microstructure of complex oxides before attempting to interpret their properties. The complexities in the compounds described above stem from the presence of two cations, Fe^{3+} and Sb^{5+}, with differences in size and charge that place them on the borderline between cation order and disorder. Only $Ca_2LaFe_2SbO_9$ can be considered to be a true, single-phase compound, albeit with some degree of compositional inhomogeneity. The barium analogue can be treated as such, although the level of inhomogeneity is sufficient to support the formation of a few ordered nanodomains within a matrix of disordered cations. In the case of $Sr_2LaFe_2SbO_9$, the inhomogeneity causes a significant degree of phase separation within the sample. The variation in the degree of cation ordering leads to a change from ferrimagnetism in $Ca_2LaFe_2SbO_9$ to

antiferromagnetism in $Ba_2LaFe_2SbO_9$. In both cases, the inhomogeneity ensures that a spin glass phase is also present.

Acknowledgments

PDB, ECH, and JH acknowledge support from EPSRC under grant EP/M0189954/1. We would also like to thank E. Suard at ILL and I. Da Silva at ISIS for the experimental assistance they provided.

References

[1] A. S. Bhalla, R. Guo, and R. Roy, *The Perovskite Structure—a Review of Its Role in Ceramic Science and Technology*, Materials Research Innovations **4**, 3 (2000).

[2] N. F. Atta, A. Galal, and E. H. El-Ads, *Perovskite Nanomaterials – Synthesis, Characterization, and Applications*, in *Perovskite Materials - Synthesis, Characterisation, Properties, and Applications*, edited by L. Pan and G. Zhu (InTech, 2016).

[3] E. A. R. Assirey, *Perovskite Synthesis, Properties and Their Related Biochemical and Industrial Application*, Saudi Pharmaceutical Journal **27**, 817 (2019).

[4] A. K. Kundu, *Magnetic Perovskites* (Springer India, New Delhi, 2016).

[5] M. T. Anderson, K. B. Greenwood, G. A. Taylor, and K. R. Poeppelmeier, *B-Cation Arrangements in Double Perovskites*, Progr in Solid State Chem **22**, 197 (1993).

[6] S. Vasala and M. Karppinen, *A2B'B"O6 Perovskites: A Review*, Progress in Solid State Chemistry **43**, 1 (2015).

[7] M. C. Knapp and P. M. Woodward, *A-Site Cation Ordering in AA'BB'O6 Perovskites*, Journal of Solid State Chemistry **179**, 1076 (2006).

[8] C. J. Howard and H. T. Stokes, *Group-Theoretical Analysis of Octahedral Tilting in Perovskites*, Acta Crystallogr B Struct Sci **54**, 782 (1998).

[9] P. M. Woodward, *Octahedral Tilting in Perovskites. I. Geometrical Considerations*, Acta Crystallogr B Struct Sci **53**, 32 (1997).

[10] P. M. Woodward, *Octahedral Tilting in Perovskites. II. Structure Stabilizing Forces*, Acta Crystallogr B Struct Sci **53**, 44 (1997).

[11] A. Hossain, A. R. Gilev, P. Yanda, V. A. Cherepanov, A. S. Volegov, K. Sakthipandi, and A. Sundaresan, *Optical, Magnetic and Magneto-Transport Properties of Nd 1-XAxMn0.5Fe0.5O3-δ (A=Ca, Sr, Ba; X=0, 0.25)*, Journal of Alloys and Compounds **847**, 156297 (2020).

[12] K. Nomura, R. Zboril, J. Tucek, W. Kosaka, S. Ohkoshi, and I. Felner, *Substitution Effects of Barium and Calcium on Magnetic Properties of AxSr1−x(Fe0.5Ru0.5)O3 Double Perovskites (X=0.05, A=Ba,Ca)*, Journal of Applied Physics **102**, 013907 (2007).

[13] K. Laajimi, M. Khlifi, E. K. Hlil, M. H. Gazzah, M. B. Ayed, H. Belmabrouk, and J. Dhahri, *Influence of Sr Substitution on Structural, Magnetic and Magnetocaloric Properties in La0.67Ca0.33−xSrxMn0.98Ni0.02O3 Manganites*, J Mater Sci: Mater Electron **31**, 15322 (2020).

[14] P. Woodward, R.-D. Hoffmann, and A. W. Sleight, *Order-Disorder in $A_2 M^{3+} M^{5+} O_6$ Perovskites*, J. Mater. Res. **9**, 2118 (1994).

[15] M. Hendrickx, Y. Tang, E. C. Hunter, P. D. Battle, J. M. Cadogan, and J. Hadermann, *CaLa2FeCoSbO9 and ALa2FeNiSbO9 (A = Ca, Sr, Ba): Cation-Ordered, Inhomogeneous, Ferrimagnetic Perovskites*, Journal of Solid State Chemistry **285**, 121226 (2020).

[16] C. Chin, P. D. Battle, E. C. Hunter, M. Avdeev, M. Hendrickx, and J. Hadermann, *Magnetic Properties of La3Ni2Sb Ta Nb1—O9; from Relaxor to Spin Glass*, Journal of Solid State Chemistry **273**, 175 (2019).

[17] P. D. Battle, S. I. Evers, E. C. Hunter, and M. Westwood, *La3Ni2SbO9: A Relaxor Ferromagnet*, Inorg. Chem. **52**, 6648 (2013).

[18] P. D. Battle, M. Avdeev, and J. Hadermann, *The Interplay of Microstructure and Magnetism in La3Ni2SbO9*, Journal of Solid State Chemistry **220**, 163 (2014).

[19] R. Paria Sena, J. Hadermann, C.-M. Chin, E. C. Hunter, and P. D. Battle, *Structural Chemistry and Magnetic Properties of the Perovskite SrLa2Ni2TeO9*, Journal of Solid State Chemistry **243**, 304 (2016).

[20] E. C. Hunter, P. D. Battle, R. Paria Sena, and J. Hadermann, *Ferrimagnetism as a Consequence of Cation Ordering in the Perovskite LaSr2Cr2SbO9*, Journal of Solid State Chemistry **248**, 96 (2017).

[21] M. S. Augsburger, M. C. Viola, J. C. Pedregosa, R. E. Carbonio, and J. A. Alonso, *Crystal Structure and Magnetism of the Double Perovskites Sr3Fe2TeO9 and Ba3Fe2TeO9: A Neutron Diffraction Study*, J. Mater. Chem. **16**, 4235 (2006).

[22] S. A. Ivanov, P. Nordblad, S.-G. Eriksson, R. Tellgren, and H. Rundlöf, *The Magnetoelectric Perovskite Sr3Fe2TeO9: An Insight from Magnetic Measurements and Neutron Powder Diffraction*, Materials Research Bulletin **42**, 776 (2007).

[23] Y. Tang, E. C. Hunter, P. D. Battle, R. P. Sena, J. Hadermann, M. Avdeev, and J. M. Cadogan, *Structural Chemistry and Magnetic Properties of the Perovskite Sr3Fe2TeO9*, Journal of Solid State Chemistry **242**, 86 (2016).

[24] H. M. Rietveld, *A Profile Refinement Method for Nuclear and Magnetic Structures*, J Appl Cryst **2**, 65 (1969).

[25] A. C. Larson and R. B. V. Dreele, *GENERAL STRUCTURE ANALYSIS SYSTEM*, 185 (n.d.).

[26] B. van Laar and W. B. Yelon, *The Peak in Neutron Powder Diffraction*, J Appl Crystallogr **17**, 47 (1984).

[27] C. J. Howard, B. J. Kennedy, and P. M. Woodward, *Ordered Double Perovskites – a Group-Theoretical Analysis*, Acta Cryst B **59**, 4 (2003).

[28] I. D. Brown and R. D. Shannon, *Empirical Bond-Strength–Bond-Length Curves for Oxides*, Acta Crystallographica Section A **29**, 266 (1973).

[29] D. I. Woodward and I. M. Reaney, *Electron Diffraction of Tilted Perovskites*, Acta Crystallogr B Struct Sci **61**, 387 (2005).

[30] D. B. Williams and C. B. Carter, *Transmission Electron Microscopy: A Textbook for Materials Science*, 2nd ed (Springer, New York, 2008).

[31] A. Faik, J. M. Igartua, E. Iturbe-Zabalo, and G. J. Cuello, *A Study of the Crystal Structures and the Phase Transitions of Sr2FeSbO6, SrCaFeSbO6 and Ca2FeSbO6 Double Perovskite Oxides*, Journal of Molecular Structure **963**, 145 (2010).

[32] M. P. Attfield, P. D. Battle, S. K. Bollen, T. C. Gibb, and R. J. Whitehead, *The Crystal Structure and Magnetic Properties of SrLaFeSnO6 and SrLaNiSbO6*, Journal of Solid State Chemistry **100**, 37 (1992).

[33] E. J. Cussen, J. F. Vente, P. D. Battle, and T. C. Gibb, *Neutron Diffraction Study of the Influence of Structural Disorderon the Magnetic Properties of Sr2FeMO6 (M=Ta,Sb)*, J. Mater. Chem. **7**, 459 (1997).

[34] N. Kashima, K. Inoue, T. Wada, and Y. Yamaguchi, *Low Temperature Neutron Diffraction Studies of Sr2FeMO6 (M=Nb, Sb)*, Appl Phys A **74**, s805 (2002).

[35] E. C. Hunter, P. D. Battle, S. J. Blundell, C. V. Topping, F. K. K. Kirschner, and F. Lang, *Muon-Spin Relaxation and AC Magnetometry Study of the Ferrimagnet LaSr2Cr2SbO9*, Journal of Solid State Chemistry **279**, 120935 (2019).

[36] C.-M. Chin, P. D. Battle, S. J. Blundell, E. Hunter, F. Lang, M. Hendrickx, R. Paria Sena, and J. Hadermann, *Comparative Study of the Magnetic Properties of La3Ni2B'O9 for B' = Nb, Taor Sb*, Journal of Solid State Chemistry **258**, 825 (2018).

[37] Y. Tang, E. C. Hunter, P. D. Battle, M. Hendrickx, J. Hadermann, and J. M. Cadogan, *Ferrimagnetism as a Consequence of Unusual Cation Ordering in the Perovskite SrLa2FeCoSbO9*, Inorg. Chem. **57**, 7438 (2018).